U.S. DEPARTMENT OF THE INTERIOR
U.S. GEOLOGICAL SURVEY

RESPONSE SPECTRA FROM THE 1989 LOMA PRIETA, CALIFORNIA, EARTHQUAKE REGRESSED FOR SITE AMPLIFICATION, ATTENUATION, AND DIRECTIVITY

by

JOHN BOATWRIGHT AND LINDA C. SEEKINS[1]

OPEN-FILE REPORT 97-858

1997

Prepared under the Cooperative Research and Development Agreement between the Pacific Gas & Electric Company and the U.S. Geological Survey for Earthquake Research in the San Francisco Bay Area.

[1] Menlo Park, CA 94025

Table of Contents

Response Spectra from the 1989 Loma Prieta, California, Earthquake Regressed for Site Amplification, Attenuation, and Directivity

John Boatwright and Linda C. Seekins

Abstract

We analyze the 5% damped pseudo-velocity response spectral ordinates obtained from 95 strong motion instruments that recorded the 1989 Loma Prieta, California, earthquake. We perform two different regressions for site amplification, attenuation, and directivity, at a set of periods from 0.04 to 10 s. The first regression uses the least distance from the rupture area to the receiver and models the directivity following Somerville et al. (1997). The second regression uses *rms* measures for the source-receiver distance and directivity that are derived from Boatwright's (1982) model for the high-frequency acceleration spectrum. The results from the two regressions are generally similar. Stations sited on bay mud are strongly amplified at periods from 0.75 to 3 s, while stations sited on competent rock are deamplified from 0.04 to 10 s. The attenuation with distance is slightly greater at periods shorter than 1 s than at longer periods. The azimuthal amplification (along-strike/fault-normal) or directivity increases gradually with period to a peak at 3 s and then decreases abruptly for longer periods. The *rms* measure of directivity used in the second regression allows us to infer an effective rupture velocity from this azimuthal amplification: the amplification of 2-3 observed for periods from 1 to 4 s corresponds to effective rupture velocities of $0.70\beta \le v \le 0.82\beta$.

Introduction

The analysis of strong motion recordings of large earthquakes has changed dramatically in the last ten years. Where previous large earthquakes were recorded by only a handful of accelerographs, the 1989 Loma Prieta, the 1994 Northridge, and the 1995 Kobe earthquakes each yielded more than 100 strong motion records in the near and intermediate field. As a consequence, the source models for these earthquakes better resolve both the rupture growth and the slip distribution at depth.

These extensive data sets and refined source models have in turn impelled an important evolution in regressions of strong motion data. Somerville et al. (1997), hereafter referred to as SSGA, recently included directivity in a comprehensive regression of velocity response spectra from twenty-one large strike-slip and dip-slip earthquakes. They regressed for directivity as a function of period, couching their results as residuals to the regression performed by Abrahamson and Silva (1997), hereafter referred to as AS. They found that directivity increases with period from $T = 0.75$ to 5 s and is stronger for strike-slip earthquakes than for dip-slip earthquakes. They found no directivity at shorter periods for these earthquakes.

In this research, we analyze the velocity response spectra from a single earthquake, the 1989 Loma Prieta earthquake, instead of the extensive sets of earthquakes that AS and SSGA consider. We compare two different regressions, the first emulating the SSGA regression and the second using *rms* measures for source-receiver distance and directivity derived from a dynamic model of the rupture process. By regressing the response spectra using these two different approaches, we can both test the interevent variability of the SSGA results and consider the dynamic implications of the SSGA directivity model.

Strong Motion Recordings of the 1989 Loma Prieta Earthquake

We have compiled the strong motion data written by the 1989 Loma Prieta earthquake. Because our regression is specific to this one earthquake, we sought to include as many recordings as possible in the regression. We evaluated recordings obtained from the basements of large buildings on a station by station basis, discarding records that appeared to be contaminated by building response. There were 119 accelerograms in the data set that we originally collected: 24 of the accelerograms obtained from buildings were discarded, either because of an apparent building response or because the building was taller than 4 stories. Two building records were retained from 3-story buildings: the VMP record from the Menlo Park VA Hospital and the PJH record from a Junior High School in Piedmont. 13 accelerograms were retained from 2-story buildings.

The stations were grouped into four separate site classes, characterized by the average shear wave velocity in the upper 30 m. These site classes are almost identical to the 1997 NEHRP site classes. Site class B has shear-wave velocities of $\beta > 750$ m/s and corresponds to competent rock, site class C has shear-wave velocities of $350 < \beta \leq 750$ m/s and corresponds to soft rock and gravely soils, site class D has shear-wave velocities of $200 < \beta \leq 350$ m/s and corresponds to deep stiff soils, while site class E has shear-wave velocities of $\beta \leq 200$ m/s and corresponds to soft soil, generally Holocene bay mud. The 200 m/s boundary between site class D and E is slightly higher than the 175 m/s NEHRP boundary, leaving both the EMV station in Emeryville and the NAS station in the Alameda Naval Air Station in site class E.

The map of the stations whose records were analyzed is shown in Figure 1. The stations extend 90 and 130 km to the southeast and northwest, respectively, along-strike from the earthquake, and about 70 km normal to the fault. This station distribution is nearly optimal for resolving directivity: the relative lack of stations to the southwest of the fault, on the Pacific plate, is compensated by an abundance of stations to the northeast. The station list compiled in Table 1 includes the station name,

location, building type, site-class, and the average shear-wave velocity in the upper 30 m. Most of these velocities are obtained by drilling boreholes and logging shear-waves down-hole; the *'s indicate stations where the shear-wave velocity is estimated from boreholes in similar geologic units.

Distance and Directivity from a Finite Fault

Regressions of strong motion data require measures of the source-receiver distance and directivity that are appropriate to the ground motion parameter analyzed. In this work, we regress velocity response spectral ordinates. We derive appropriate measures of distance and directivity by considering Boatwright's (1982) model for the acceleration amplitude spectrum of far-field S-waves.

Madariaga (1977) analyzed the waves radiated by rupture fronts that abruptly change velocity. Boatwright (1982) extended this analysis to model the far-field acceleration amplitude spectra radiated by a subevent or a set of subevents within an earthquake. He showed that the high-frequency acceleration spectral level scales as

$$|\ddot{u}(\omega)| \propto \frac{D(v/\beta, \vartheta)}{r} \Delta\sigma \Sigma^{1/2} \tag{1}$$

where r is the hypocentral distance, $\Delta\sigma$ is the dynamic stress drop, and Σ is the rupture area. The function

$$D(v/\beta, \vartheta) = \left(1 - \frac{v}{\beta}\cos\vartheta\right)^{-1} \tag{2}$$

is the Ben-Menahem (1970) directivity function, which depends on the ratio of the rupture velocity v to the S-wave velocity β, and the angle ϑ between the rupture direction and the takeoff direction of the S-wave. To obtain equation (1), we disregard the azimuthal variations of both the S-wave radiation pattern and the diffraction effects discussed by Boatwright (1982), and presume that the far-field term dominates the radiated acceleration, even in the near-field.

Because the phase shifts between the acceleration pulses radiated by different parts of the rupture area are effectively random, the contributions to the acceleration amplitude spectra, or equivalently, the velocity response spectra, should be summed incoherently, that is, by summing the radiated power spectra (see Lee, 1964, p. 240-244). We write this incoherent summation as the integral

$$|\ddot{u}(\omega)|^2 \propto \int \frac{\Delta\sigma^2 D^2(v/\beta, \vartheta)}{r^2} d\Sigma \tag{3}$$

and assume that the dynamic stress drop is approximately constant over the rupture area Σ.

Most ground motion regressions use the least distance from the receiver to the rupture area r_{min} (Sadigh et al., 1993), or the least distance from the receiver to the surface projection of the rupture area x_{min} (Boore et al., 1997). These definitions of source-receiver distance imply that the seismic source acts as though it were concentrated at the closest point of the rupture area to the receiver. AS introduce a hyperdepth, h, in their definition of the source-receiver distance,

$$r_{AS} = \left(r_{min}^2 + h^2\right)^{1/2}, \tag{4}$$

and obtain $3.5 \le h \le 5.6$ in their regressions of horizontal response spectral ordinates from 5 to 0.05 s.

In contrast, the integral in equation (3) suggests that an appropriate source-receiver distance can be calculated from the integral of $1/r^2$ over the rupture area Σ,

$$\left\langle \frac{1}{r} \right\rangle^2 = \frac{1}{\Sigma} \int \frac{d\Sigma}{r^2}. \tag{5}$$

This measure of source-receiver distance from a finite fault is the inverse of the *rms* inverse distance to the rupture area. We will write it formally as $\langle 1/r \rangle^{-1}$ but refer to it informally as the *rms* distance.

Figure 2 plots the least distance to the rupture area against the *rms* distance for the 95 stations in the Loma Prieta data set. The upper limit of the plotted points corresponds to the stations close to the fault normal while the lower limit corresponds to the stations along the fault strike. The critical difference occurs at small distances, where $\langle 1/r \rangle^{-1}$ approaches 10 km as r_{min} approaches 0 and r_{AS} approaches h. We used a hypocenter depth of $h = 3.5$ to compare these two measures.

We consider two different measures of directivity. SSGA key their measure of directivity to the function $\cos \vartheta_h$, where ϑ_h is the angle between the horizontal takeoff angle from the hypocenter to the receiver and the fault strike. To accommodate faults that rupture asymmetrically, they multiply $\cos \vartheta_h$ by $X = s/L$, where s is the distance along strike from the hypocenter to the receiver (less than or equal to the fault extent in that direction) and L is the total fault length, yielding

$$X \cos \vartheta_h = \frac{s}{L} \cos \vartheta_h \tag{6}$$

as their measure of directivity. For a unilateral fault, $X \cos \vartheta_h \equiv 0$ in the "back" half of the focal sphere and increases to $X \cos \vartheta_h = 1$ along the fault strike in the direction of rupture. For a bilateral fault, $X \cos \vartheta_h = 0$ only on the fault normal and increases to $X \cos \vartheta_h = 0.5$ in both directions along the fault strike.

The integral for the acceleration power spectrum suggests a different approach. We calculate the *rms* directivity function as

$$\langle D(v/\beta) \rangle^2 = \frac{1}{\langle 1/r \rangle^2 \Sigma} \int \frac{D^2(v/\beta, \vartheta)}{r^2} d\Sigma \tag{7}$$

assuming that the rupture velocity is a constant fraction of the S-wave velocity, v/β. Both the shape and the amplitude of the directivity function are determined by the rupture velocity. Evaluating this integral requires that we specify the rupture direction and takeoff angle everywhere on the rupture area: we use the direction from the hypocenter to the incremental fault area $d\Sigma$ and a layered velocity structure to "bend" the vertical takeoff angle.

Taken together, these measures of *rms* distance and directivity reduce the integral for the acceleration amplitude spectral level to

$$|\ddot{u}(\omega)| \propto \left\langle \frac{1}{r} \right\rangle \langle D(v/\beta) \rangle \Delta\sigma \Sigma^{1/2} \tag{8}$$

which is readily linearized by taking logarithms. We note that this decomposition is not unique: other choices for either the source-receiver distance or directivity are possible. The decomposition obtained through equations (5) and (7) is relatively simple, however, in that the rupture propagation affects only the $\langle D(v/\beta) \rangle$ term.

To compare this measure of directivity with the $X \cos\vartheta_h$ function used by SSGA, we set $\langle D(v/\beta) \rangle$ equal to the Ben-Menahem (1970) directivity function and solve for the corresponding value of $\cos\vartheta$, which we write as

$$\langle \cos\vartheta \rangle = \frac{\beta}{v} \left(1 - \langle D(v/\beta) \rangle^{-1} \right) . \tag{9}$$

Although $\langle \cos\vartheta \rangle$ depends on the assumed rupture velocity, the term in parenthesis makes this dependence weaker than v^{-1}.

Figure 3 plots $X \cos\vartheta_h$ against $\langle \cos\vartheta \rangle$ for the 95 stations in the Loma Prieta data set. Because the earthquake rupture was almost exactly bilateral, $X \cos\vartheta_h \leq 0.51$: in contrast, $\langle \cos\vartheta \rangle \leq 0.81$. The greatest variation between these two measures occurs for stations near the rupture area: the $X \cos\vartheta_h$ measure considers only the horizontal component of rupture while the $\langle \cos\vartheta \rangle$ measure incorporates the 2D aspect of the faulting process. We do not consider the $Y \cos\varphi_h$ measure of updip directivity that SSGA incorporate in their regression.

Regression Results

We run two different regressions on the Loma Prieta data: both regressions incorporate directivity. The first regression approximates the scheme used by AS, as extended to include directivity by SSGA. We fit

the logarithms of the velocity response spectral ordinates R_{ji} for the station j independently at each period i as

$$\ln R_{ji} = \ln \Omega_i - \gamma_i \ln r_{ASj} + \ln \delta_{ki} + \left(X \cos \vartheta_h\right)_j \ln D_i \qquad (10)$$

regressing for the average source excitation, Ω_i; the geometrical spreading exponent, γ_i; the relative amplification, δ_{ki}, of the kth site-class, and the directivity factor, D_i. Here r_{ASj} is the AS distance to station j, $k(j)$ is the site-class for station j, and $\left(X \cos \vartheta_h\right)_j$ is the directivity measure.

The regression is demonstrated in Figures 4a-4c, using the response spectral ordinates at 3.0 s as an example. The spectral ordinates at this period had the strongest directivity in the data set. Figure 4a plots the spectral ordinates as a function of distance, gathered by site class. Figure 4b plots the spectral ordinates as a function of distance, corrected for site-class and directivity. Finally, Figure 4c plots the spectral ordinates as a function of source-receiver azimuth, corrected for distance and site-class.

The regression results are compiled as functions of period in Figures 5-7, which show γ_i, D_i, and δ_{ki}, respectively. The estimates of γ_i at periods less than 1 Hz are about 0.2 lower than the estimates obtained by AS from their regression of 58 earthquakes. The sag in γ_i estimates at 0.75 and 1 s may reflect the "Moho bounce" observed in the Loma Prieta data at distances around 100 km northwest from the epicenter (Somerville et al., 1990). A significant amplification at this distance would decrease the apparent attenuation. At longer periods, the estimates of γ_i approximate the estimates obtained by AS, although there is some variability above 5 s.

The directivity factors D_i are plotted in Figure 6: the factors at periods less than 3 s are slightly larger than the directivity factors obtained by SSGA, but they clearly behave similarly as a function of period. At periods longer than 3 s, the directivity factors decrease abruptly. These results indicate that directivity depends strongly on period but suggest that the period at which the directivity is strongest may be different for

each earthquake. Because the directivity is modeled as $D_i^{X\cos\vartheta_h}$ and $(X\cos\vartheta_h)_j \le 0.5$ for a perfectly bilateral fault, the regressed directivity factors D_i are the square of the azimuthal amplification (along-strike/fault-normal) observed in the data.

Because all of the more distant stations ($r_{AS} > 70$ km) are situated along strike, the directivity trades off with the attenuation. To illustrate this tradeoff, we repeat the regression of the Loma Prieta response spectra, constraining the attenuation at each period to equal the attenuation obtained by AS and plotted as triangles in Figure 5. The resulting directivity factors are plotted as diamonds in Figure 6. Differences of $d\gamma_i = \pm 0.1$ yield variations of $\pm 20\%$ in $D_i^{1/2}$, so that the directivity is increased.

The amplifications relative to site class C are plotted together in Figure 7. These results are marked by relatively low amplitudes for site class B, the stations on competent rock, at all periods, and by the large amplitudes for site class E, the stations on Holocene bay mud, for $T = 0.5$ to 3 s. Site class E is amplified by factors of 3-4 over site class B at these periods. The consistent deamplification ($\delta_{Bi} \approx 0.7$) of site-class B relative to site-class C at all periods is somewhat surprising.

The second regression uses the *rms* measures of source-receiver distance and directivity derived in the last section to fit

$$\ln R_{ji} = \ln \Omega_i + \gamma_i \ln\left\langle \frac{1}{r} \right\rangle_j + \ln \delta_{ki} + \ln\langle D(v/\beta)\rangle_j + \delta(v/\beta)\frac{d\ln\langle D(v/\beta)\rangle_j}{d(v/\beta)} \qquad (11)$$

for the average source excitation, Ω_i; the geometrical spreading exponent, γ_i; the relative amplifications, δ_{ki}, and the rupture velocity, (v/β). This regression is computationally similar to the regression in equation (10), except that we solve iteratively for (v/β) using a Taylor Series expansion with the derivative

$$\frac{d\ln\langle D(v/\beta)\rangle_j}{d(v/\beta)} = \int \frac{\cos\vartheta}{r^2} D^3(v/\beta,\vartheta)\,d\Sigma \Big/ \int \frac{D^2(v/\beta,\vartheta)}{r^2}\,d\Sigma \qquad (12)$$

and the positivity constraint $(v/\beta) \ge 0$.

The results from the second regression strongly resemble the results from the first regression. The relative amplitudes for the different site classes are almost identical: we have not plotted the relative amplifications from the second regression. The second regression fits the velocity response spectral ordinates slightly better, by about one part in 100.

The largest differences between the two regressions occur in the estimates of γ_i. Figure 8 shows that the γ_i's from the second regression are much closer to the γ_i's obtained by AS from the larger set of earthquakes. These estimates of γ_i are physically reasonable, where $\gamma_i \cong 1.1$-1.0 for $T \leq 0.2$s correspond to body-wave propagation with some anelastic attenuation, and $\gamma_i \cong 0.6$-0.8 for $T > 1$ s correspond to surface-wave propagation. The "sag" at 0.75 and 1.0 s is more pronounced in the estimates of γ_i from the second regression.

Figure 9 depicts the azimuthal amplification by comparing the response spectral ordinates inferred for a station at $\langle 1/r \rangle^{-1} = 10$ km along-strike ($\langle \cos \vartheta \rangle = 0.8$) to those inferred for a station at $\langle 1/r \rangle^{-1} = 10$ km on the fault-normal ($\langle \cos \vartheta \rangle = 0$). The separation between the two curves indicates the azimuthal amplification caused by the rupture directivity. The amplification is 2 or more for $0.4 \leq T \leq 4.0$ s, and 3 or more for $1.5 \leq T \leq 3.0$ s. This increase relative to the directivity factors plotted in Figure 6 is derived from the different measures of source-receiver distance: because $r_{AS} < \langle 1/r \rangle^{-1}$ for stations along the fault strike, the apparent directivity is muted in the SSGA regression.

The directivity is plotted directly in Figure 10, where the right-hand ordinate indicates the rupture velocity (v/β) and the left-hand ordinate indicates the peak amplification

$$D_{max} = \left(1 - \frac{v}{\beta}\right)^{-1} \tag{13}$$

that is, the amplification for a station with $\langle \cos \vartheta \rangle = 1$. The variation as a function of period is similar to the variation in Figure 6: the amplification increases with period up to T=3 s and then abruptly decreases for periods T> 3 s.

Iterating the regression in equation (11) until $\delta(v/\beta) = 0$ yields an apparently period-dependent rupture velocity. We use the term "effective rupture velocity" because it is unclear what aspect of the rupture process varies with period. The directivity observed in the response spectra for the periods $1.5 \leq T \leq 4.0$ s corresponds to effective rupture velocities in the range $0.7\beta \leq v \leq 0.82\beta$.

Discussion

We begin our discussion by considering Figure 6, which compares the directivity factors obtained from the first regression (both with and without constraining the attenuation to the results obtained by AS) against the directivity factors obtained by SSGA from their regression of 21 large earthquakes. The three sets of directivity factors share a similar behavior as a function of period, increasing markedly with period for $T \geq 2$ s. Although generally within the derived uncertainties, the directivity factors from the Loma Prieta regressions are 20% and 60% larger than those from the SSGA regression. How do we understand this difference?

One possible explanation is that the Loma Prieta earthquake is an anomalous event with stronger directivity than the average earthquake in the set of large events that SSGA regress. The Loma Prieta earthquake caused significant damage in municipalities situated along the fault strike, such as San Francisco, Oakland, and Watsonville. However, the rupture velocities that have been inferred by inverting the radiated waveforms are almost all in the range of $0.75\beta \leq v \leq 0.85\beta$ (see Beroza (1991), Steidl and Archuleta (1991), Wald et al. (1991), among many others). This range of rupture velocity is seismologically unremarkable, and corroborates the effective rupture velocities obtained in Figure 10.

The directivities plotted in Figures 6 and 10 suggest another explanation for the discrepancy between our results and those of SSGA. The directivity varies systematically as a function of period, increasing with period to a peak at the period most strongly enhanced by the directivity.

Applying the analysis of Boatwright (1984) to the Loma Prieta earthquake shows that the directivity peak at $T = 2$-3 s corresponds to a half-cycle of velocity with $\tau_{1/2} = 1.0$-1.5 s. The rupture length of $L = 20$ km and the inferred rupture velocity of $v = 3$ km/s yields a rupture duration of $L/v = 6$-8 s. In the direction of rupture, directivity foreshortens this duration by a factor of 4-5. Clearly, the period of this peak should vary linearly with the rupture extent along strike from the hypocenter to the stations.

This variation with period occurs not only for earthquakes of different rupture lengths, but also for earthquakes with different rupture extents, that is, earthquakes that are asymmetric but not unilateral. As the rupture becomes more asymmetric, the peaks in the two directions along strike will split in period, broadening the shape and reducing the maximum directivity. Bilateral ruptures like the 1989 Loma Prieta earthquake should have the strongest possible directivity, because the period dependence is the same in both directions along strike.

Conclusions

We have regressed the strong motion recordings of the 1989 Loma Prieta earthquake for site amplification, attenuation, and directivity using two different regressions. These regressions share the same structure, but use different measures of source-receiver distance and directivity: the first emulates the regression of Abrahamson and Silva (1997), as modified to consider directivity by Somerville et al. (1997); the second uses *rms* measures of distance and directivity. The results from the two regressions are nearly identical for the relative amplifications, differ slightly for the attenuation with distance, and differ only by a small factor for the directivity.

The directivity obtained from these regressions is strongly peaked at periods of 2-3 s, corresponding to twice the pulse width expected along strike from the Loma Prieta earthquake. The peak amplification of $D_{max} \cong 5.6$ in turn corresponds to an effective rupture velocity of

$v = 0.82\beta$, well within the range of rupture velocities used by Beroza (1990) and Steidl and Archuleta (1990) in their analysis of the velocity waveforms. The observed azimuthal amplification (along-strike/fault-normal) of 2-3 for periods from 1-4 s is significant for seismic engineering purposes.

Comparing the analyses and results from these two regressions gives some insight into the results obtained by SSGA from their regression of 21 large earthquakes. In particular, the marked dependence of the Loma Prieta directivity on period makes SSGA's assumption that directivity is a fixed function of period appear problematic. It is possible that performing a simultaneous regression of these 21 earthquakes has yielded a somewhat low estimate for the average directivity: a more conservative approach might regress for the directivity associated with each earthquake individually.

Pioneering papers like Somerville et al. (1997) are often greeted with undue criticism and unwarranted revisionism. To first order, our comparisons between the different regression schemes strongly corroborate their results. The largest differences are derived from the different measures of source-receiver distance. Regardless of the difficulties of designing regressions appropriate for multi-event data sets, it is clear that the SSGA paper marks a critical watershed for modeling strong ground motion.

Acknowledgments

We would like to thank Dave Boore for his continual help with data requests and questions throughout the course of this research, and Paul Spudich, Bill Joyner, and Woody Savage for their insightful reviews. Comments by Norm Abrahamson and a brief conversation with Paul Somerville helped to focus our analysis. This research was supported by the Cooperative Research and Development Agreement between the Pacific Gas & Electric Company and the U.S. Geological Survey on Earthquake Hazards in the San Francisco Bay Area.

Bibliography

Abrahamson, N.A., and W.J. Silva, (1997). Empirical response spectral relations for shallow crustal earthquakes, *Seism. Res. Letters*, **68**, 94-127.

Ben-Menahem, A., (1961). Radiation of seismic surface waves from finite moving sources, *Bull. Seism. Soc. Am.*, **51**, 401-435.

Beroza, G.C., (1991). Near-source modeling of the Loma Prieta earthquake; evidence for heterogeneous slip and implications for earthquake hazard, *Bull. Seism. Soc. Am.*, **81**, 1603-1621.

Boatwright, J., (1982). A dynamic model for far-field acceleration, *Bull. Seism. Soc. Am.*, **72**, 1049-1068.

Boatwright, J., (1984). The effect of rupture complexity on estimates of source size, *J. Geophys. Res.*, **89**, 1132-1146.

Boore, D.M., W.B. Joyner, and T.E. Fumal, (1997). Equations for estimating horizontal response spectra and peak accelerations from western North American earthquakes: a summary of recent work, *Seism. Res. Letters*, **68**, 128-153.

Lee, Y.W., (1964). *The Statistical Theory of Communication*, John Wiley and Sons, Inc., New York.

Madariaga, R., (1977). High-frequency radiation from crack (stress drop) models of earthquake faulting, *Geophys. J.*, **51**, 55-62.

Sadigh, K, C-Y Chang, N.A. Abrahamson, S.J. Chiou, and M. Power, (1993). Specification of long period motions: updated attenuation relations for rock site conditions and adjustment factors for near-fault effects, Proc. ATC 17-1, 59-70.

Somerville, P.G., N.F. Smith, R.W. Graves, and N.A. Abrahamson, (1997). Modification of empirical strong ground motion attenuation relations in include amplitude and duration effects of rupture directivity, *Seism. Res. Letters*, **68**, 199-222.

Somerville, P.G., and J. Yoshimura, (1990). The influences of critical Moho reflections on strong ground motion recorded in San Francisco and Oakland during the 1989 Loma Prieta earthquake, *Geophys. Res. Letters.*, **17**, 1203-1206.

Steidl, J.H., R.J. Archuleta, and S.H. Hartzell, (1991). Rupture history of the 1989 Loma Prieta, California, earthquake, *Bull. Seism. Soc. Am.*, **81**, 1573-1602.

Wald, D.J., D.V. Helmberger, and T.H. Heaton, (1991). Rupture model of the 1989 Loma Prieta earthquake from the inversion of strong-motion and broadband teleseismic data, *Bull. Seism. Soc. Am.*, **81**, 1540-1572.

Table 1 - Station List

Station	Lat W	Long N	Structure	Operator	SC	β m/s	Site
A01	37.550	122.230	FF	CDMG	D	112	C,E
A02	37.520	122.250	FF	USGS	D	134	C,E,F
A09	37.470	122.320	FF	USGS	B	454	A,C
A10	37.465	122.343	FF	CDMG	B	401	A,C
A2E	37.657	122.082	1-St	CDMG	C	276	A,C
A3E	37.657	122.061	FF	CDMG	B	522	A,C
AGW	37.397	121.952	1-St	CDMG	C	264	A,C
AND	37.166	121.628	Dam DS	USGS	B	525	A,C,H
BKS	37.870	122.240	FF	Bky/USGS	B	507	C*
BLM	37.512	122.308	2-St	CDMG	B	628	A,C,F
BVF	36.573	121.184	1-St	USGS	C	266	B*
CAP	36.974	121.952	1-St	CDMG	C	289	A,C,F
CDS	37.529	122.361	Dam DS	CDMG	B	507	A*
CFH	37.780	122.510	2-St	CDMG	A	1076	C*
CLS	37.046	121.803	1-St	CDMG	B	460	A,E,F
CRS	37.452	121.807	1-St	USGS	B	482	A,E,H
CRY	37.396	121.756	FF	USGS	A	1076	A,C*
CYC	37.118	121.550	FF	CDMG	B	650	B*
CYD	37.124	121.551	Dam DS	CDMG	B	507	A,C*
DFS	37.709	121.932	1-St	USGS	C	266	A,C*
DMH	37.740	122.430	2-St	CMDG	B	584	A,C,F
DVD	37.615	121.745	Dam Toe	DWR/USGS	A	1076	B*
EMV	37.844	122.295	FF	USGS	C	200	C,G
FCY	37.555	122.248	2-St	USGS	D	125	C,G
FMS	37.535	121.929	1-St	USGS	C	283	A,C,G
G01	36.973	121.572	FF	CDMG	A	1415	A,C
G02	36.982	121.556	1-St	CDMG	C	309	A,C,D,F
G03	36.987	121.536	1-St	CDMG	C	306	A,C
G04	37.005	121.522	1-St	CDMG	C	223	A,C
G06	37.026	121.484	1-St	CDMG	B	714	A,C
G07	37.033	121.434	1-St	CDMG	C	333	A,C,E,F
GCR	36.673	121.195	2-St	USGS	B	391	A,C,H
GIL	36.973	121.568	1-St	CDMG	B	507	A,C*
GOF	37.009	121.569	2-St	CDMG	B	507	A,C*
HCH	36.851	121.402	1-St	USGS	C	266	A,C
HDA	36.888	121.413	FF	USGS	C	218	A,C,H

HVR	37.338	121.714	FF	CDMG	C	265	A,C,F
HWC	37.679	122.082	FF	USGS	B	735	A,C*
LEX	37.202	121.949	Dam LA	CDMG	A	1071	C,F
LFT	37.946	122.508	Deck	USGS	D	173	C,G
LOB	37.001	122.060	1-St	CDMG	B	507	A,C,F
MCH	36.597	121.897	1-St	CDMG	A	763	A,C,F
MIL	37.430	121.897	2-St	CDMG	C	266	A,C*
MSJ	37.530	121.919	1-St	CMDG	B	368	A,C
MZD	38.017	122.183	Dam Toe	BuRec	B	507	I
NAS	37.785	122.303	1-St	USN/USGS	E	175	A,D
OFB	37.806	122.267	2-St	CDMG	C	323	A,C,E
OHW	37.816	122.314	Deck	CDMG	C	251	A,C,D
OND	37.090	121.038	Dam Toe	BuRec	C	266	I
PHT	37.790	122.430	2-St	CDMG	A	1250	A,F
PJH	37.823	122.233	3-St	CDMG	A	896	A,C,F
PNM	36.483	121.180	1-St	USGS	A	1076	A,C*
POF	37.453	122.112	2-St	CDMG	C	207	A,C,E,F
PRH	38.043	122.797	FF	CDMG	B	507	C*
PRS	37.792	122.457	FF	CDMG	B	594	C,E,F
PTB	37.820	122.520	1-St	USGS	A	1316	C,F
RCH	37.935	122.342	FF	CDMG	C	260	C*
RIN	37.790	122.390	FF	CDMG	A	872	C
SAF	37.728	122.385	1-St	USGS	A	1076	A,C*
SAL	36.671	121.642	1-St	CDMG	C	266	A,C*
SAR	37.262	122.009	1-St	CDMG	B	507	A,C*
SFG	37.806	122.472	Br Ab	USGS	B	507	C*
SFO	37.622	122.398	1-St	CDMG	C	224	A,C,D
SG3	36.753	121.396	FF	CDMG	B	507	A,C,F
SGI	36.765	121.446	Vault	USGS	A	1076	A,C*
SJD	36.817	121.446	Dam Toe	BuRec	B	507	I
SJH	37.340	121.851	Hwy Ab	CDOT/USGS	C	266	B*
SLA	37.419	122.205	1-St	SU/USGS	C	266	A,C,G
SLD	37.058	121.075	Dam Toe	BuRec	C	266	I
SNF	37.597	121.880	1-St	USGS	B	405	A,C,H
STG	37.255	122.031	1-St	CDMG	B	507	A,C*
STH	37.210	121.803	FF	CDMG	A	1076	A*
SVL	37.402	122.024	1-St	USGS	C	268	A,G
TRI	37.825	122.373	2-St	CDMG	D	171	C,D,F
UBR	36.569	121.043	1-St	USGS	C	266	B*
VMP	37.468	122.157	3-St	VA/USGS	C	275	B*

WBR	36.532	121.143	1-St	USGS	C	311	A,C,H
WDS	37.429	122.258	1-St	CDMG	B	455	A,C,E,F
WMR	36.658	121.249	1-St	USGS	C	330	A,C,H
XBRN	37.047	121.985	1-St	UCSC	B	507	B*
XDUM	37.492	122.136	FF	CDMG	D	143	B*
XHAY	37.670	122.086	FF	CDMG	B	507	A,C*
XHOL	36.848	121.397	FF	CDMG	C	266	C*
XLBL	37.876	122.249	FF	CDMG	B	507	C*
XLGP	37.172	122.010	1-St	UCSC	B	507	B*
XLL1	37.687	121.701	FF	LLNL	B	507	C*
XLL2	37.693	121.714	FF	LLNL	B	507	C*
XLL3	37.702	121.684	FF	LLNL	B	507	C,F
XLL4	37.674	121.704	FF	LLNL	B	507	C*
XLL5	37.629	121.497	FF	LLNL	B	507	C*
XSPG	37.433	122.168	2-St	SU/USGS	B	507	B*
XSSF	37.674	122.388	FF	CDMG	A	1020	A,C,F
XUCR	37.490	122.310	FF	CDMG	B	435	B*
XWAH	36.973	121.995	2-St	UCSC	B	507	B*
YBI	37.810	122.360	1-St	CDMG	A	1076	A,C,D

Structure-Type Instrumented

FF	Free Field
1-St	One Story Building
2-St	Two Story Building
3-St	Three Story Building
Dam Toe	Dam - Toe
Dam LA	Dam - Left Abutment
Dam DS	Dam - Downstream
Hwy Ab	Highway Abutment
Br Ab	Bridge Abutment
Vault	Seismic Vault
Deck	Ferry Building Deck

References for Site Classification

A	Boore et al. (1997)
B	Pers. Comm., Tom Fumal
C	Open-File 91-311
D	Open-File 92-276
E	Open-File 93-276
F	Open-File 93-502
G	Open-File 94-222
H	Open-File 94-552
I	Bureau of Reclamation
*	velocity estimated rather than directly measured

Figure Captions

Figure 1. Map of the extended San Francisco Bay Area showing the locations of the 95 stations whose recordings are analyzed. The surface projection of the rupture area of the Loma Prieta earthquake is indicated by the shaded rectangle. The site classes for the stations are indicated by the color of the station label: site-class B (competent rock) is blue, site-class C (soft rock and gravely soils) is green, site-class D (sand and deep soils) is orange, and site-class E (bay mud) is red.

Figure 2. Abrahamson and Silva's (1997) definition of source-receiver distance, r_{AS}, plotted against *rms* distance for 65 of the 95 stations that were used. The lower limit of the distribution corresponds to stations located along the strike of the fault, while the upper limit corresponds to stations located normal to the fault. The stations at distances greater than 70 km lie near the fault strike and plot along the lower limit of the distribution.

Figure 3. The $X\cos\vartheta_h$ measure of directivity derived by SSGA plotted against the *rms* measure of directivity $\langle\cos\vartheta\rangle$ derived in equations (7) and (9) for the 95 stations analyzed. The cluster of stations with $X\cos\vartheta_h \cong 0.5$ lie along the fault strike. The variation between these directivity measures at small values of $\langle\cos\vartheta\rangle$ largely derives from the purely horizontal definition of $X\cos\vartheta_h$: the eleven labelled stations are relatively close to the fault.

Figure 4a. Response spectral ordinates at 3 s, gathered by site class and plotted as a function of r_{AS} distance. The solid lines show the fit to each site class, while the dashed lines show the uncertainty of the fits (±one standard deviation). The jagged lines show running averages, averaged over 16 km. The shear wave velocities written on each plot are the average for the specific set of stations. The amplification relative to site-class C and the normalized variance is indicated for each site-class. Figure 4b. Site response spectral ordinates, corrected for site class and directivity following equation (10) and plotted as a

function of r_{AS} distance. The composite symbols indicate stations to the SE of the epicenter (all of the site-class E stations are to the NW). The fitted directivity factor and the normalized variance for the station set are written on the plot. Figure 4c. Site response spectral ordinates, corrected for site class and distance to $r_{AS} = 30$ km following equation (10), plotted as a function of station azimuth from the receiver. The composite symbols indicate stations with $r_{AS} > 70$. The fit to the directivity, drawn as a solid curve, is controlled by the large values near N35°W and the small values near the normals to the fault.

Figure 5. Attenuation from the first regression, plotted as a function of period. The octagons are the attenuation exponents obtained from the regression in equation (10), while the triangles are the attenuation exponents obtained by AS from their regression of response spectra from 58 large earthquakes. Note the sag in the estimates of γ_i at $T =$ 0.75 and 1.0 s: this sag may result from the Moho reflection observed in the data recorded in San Francisco and Oakland.

Figure 6. Directivity factors from the first regression, plotted as a function of period. The octagons are the directivity factors obtained from the regression in equation (10): the diamonds are the directivity factors obtained by regressing the Loma Prieta data with the attenuation constrained to the average attenuation determined by AS that is plotted in Figure 5. Both estimates of directivity are peaked at 2-3 s. The triangles are the directivity factors obtained by SSGA from their regression of the response spectra from 21 large earthquakes. The right hand label for the plot indicates the scale for the directivity factors as regressed from equation (10), while the left hand label for the plot indicates the amplification observed in the Loma Prieta data.

Figure 7. Site-class amplification relative to site-class C obtained from the first regression, plotted as a function of period. The dashed line at 1.0 represents the amplification of site-class C. Site-class E (bay mud) is strongly amplified for the periods around 1 Hz, while site-class B (competent rock) is deamplified at all periods.

Figure 8. Attenuation exponents plotted as a function of period. The octagons are the attenuation exponents obtained from the regression in equation (11). The triangles are the attenuation exponents obtained by AS from their regression of response spectra from 58 large earthquakes. The sag at 0.75 and 1.0 Hz is more pronounced for this regression.

Figure 9. Azimuthal amplification plotted as a function of period. The octagons are the source spectra Ω_i, scaled to a distance of $\langle 1/r \rangle^{-1} = 10$ km, obtained from the regression in equation (11). The diamonds are the spectra for $\langle \cos \vartheta \rangle = 0.8$, estimated as an average from the data. The azimuthal amplification is the ratio between these source spectral estimates, that reaches factors of 2-3 at the periods from 0.4 to 4.0 s.

Figure 10. Directivity factors plotted as a function of period. The octagons are the directivity factors D_{max} obtained from the regression in equation (11). The left hand side of the plot indicates the scale for the peak directivity $D_{max} = (1 - v/\beta)^{-1}$, while the right hand side indicates the scale for the effective rupture velocity v/β. The directivity factors obtained for 1-4 s are commensurate with effective rupture velocities of $0.7\beta \leq v \leq 0.82\beta$.

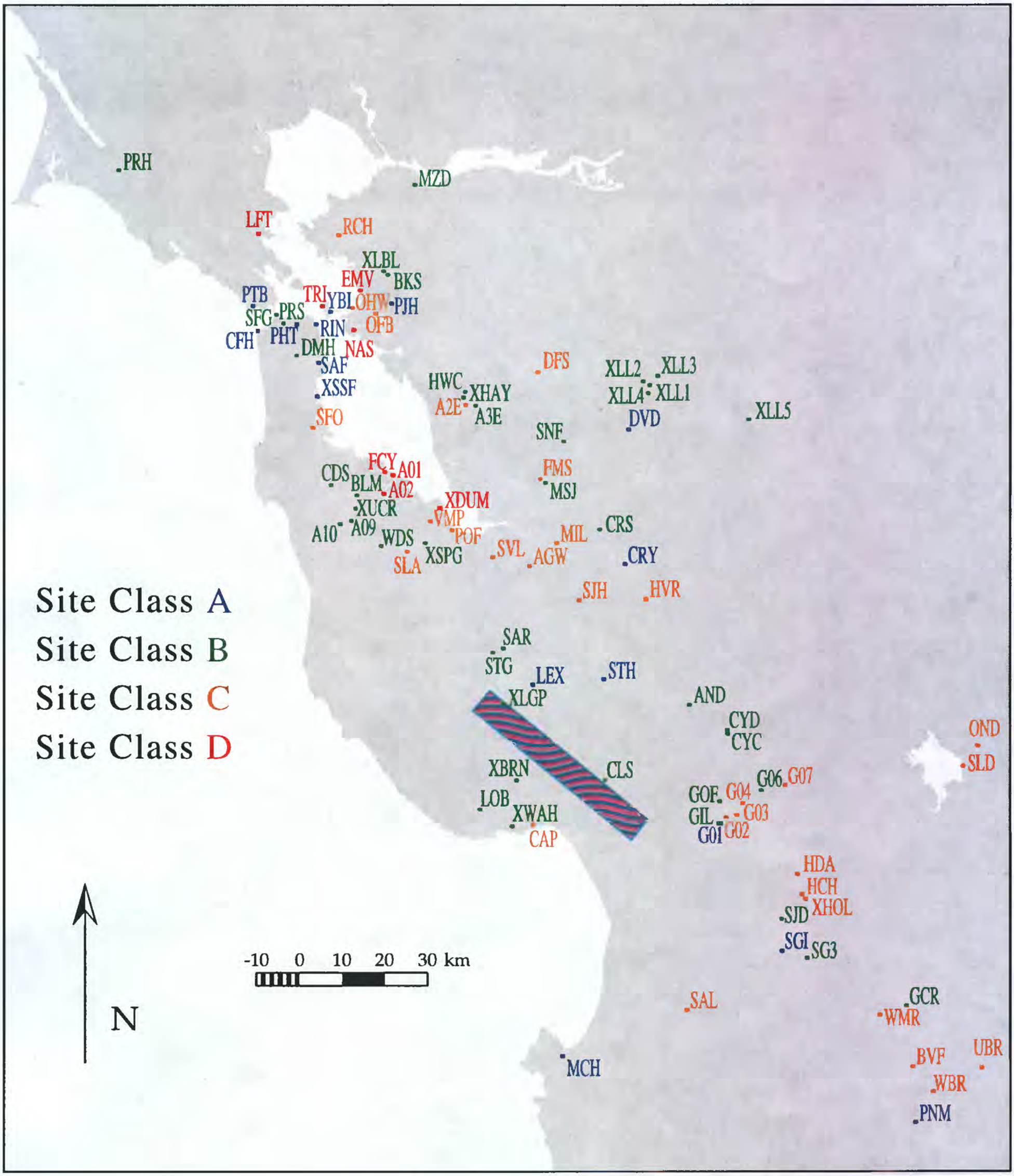
PRH
MZD
LFT
RCH
XLBL
EMV
BKS
PTB
TRI
YBL
OHW
PJH
SFG
PRS
RIN
OFB
CFH
PHT
DMH
NAS
SAF
XSSF
SFO
DFS
XLL2
XLL3
HWC
XHAY
XLL4
XLL1
A2E
A3E
DVD
XLL5
SNF
FCY
A01
CDS
BLM
A02
FMS
MSJ
XUCR
XDUM
VMP
A10
A09
WDS
POF
MIL
CRS
SVL
AGW
CRY
SLA
XSPG
SJH
HVR
SAR
STG
LEX
STH
XLGP
AND
CYD
CYC
OND
SLD
XBRN
CLS
G06
G07
GOF
G04
G03
LOB
XWAH
GIL
G01
G02
CAP
HDA
HCH
XHOL
SJD
SGI
SG3
SAL
GCR
WMR
MCH
BVF
UBR
WBR
PNM
Site Class A
Site Class B
Site Class C
Site Class D
-10 0 10 20 30 km
N

Figure 1

Loma Prieta - Distance Measures

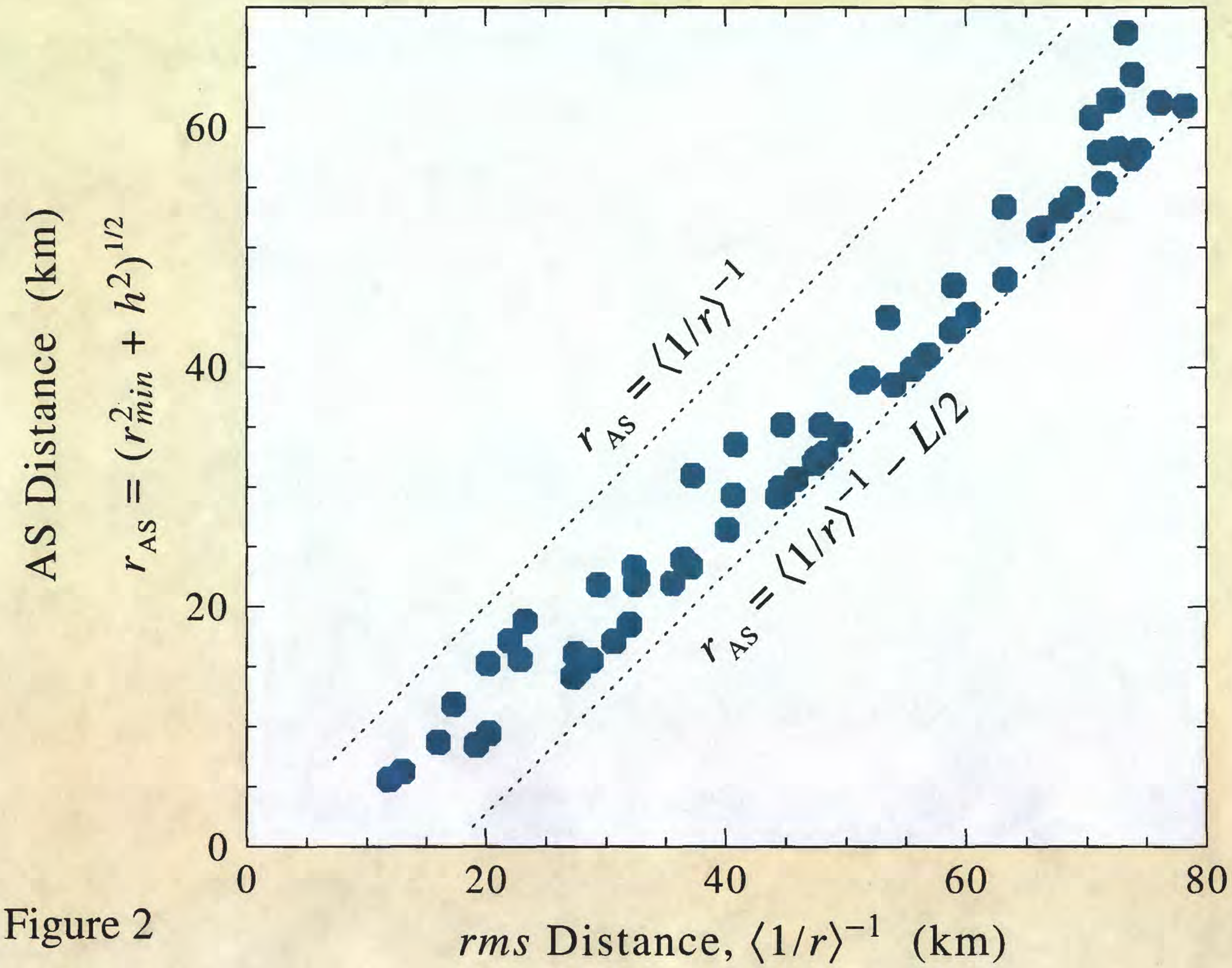

Figure 2

Loma Prieta - Directivity Measures

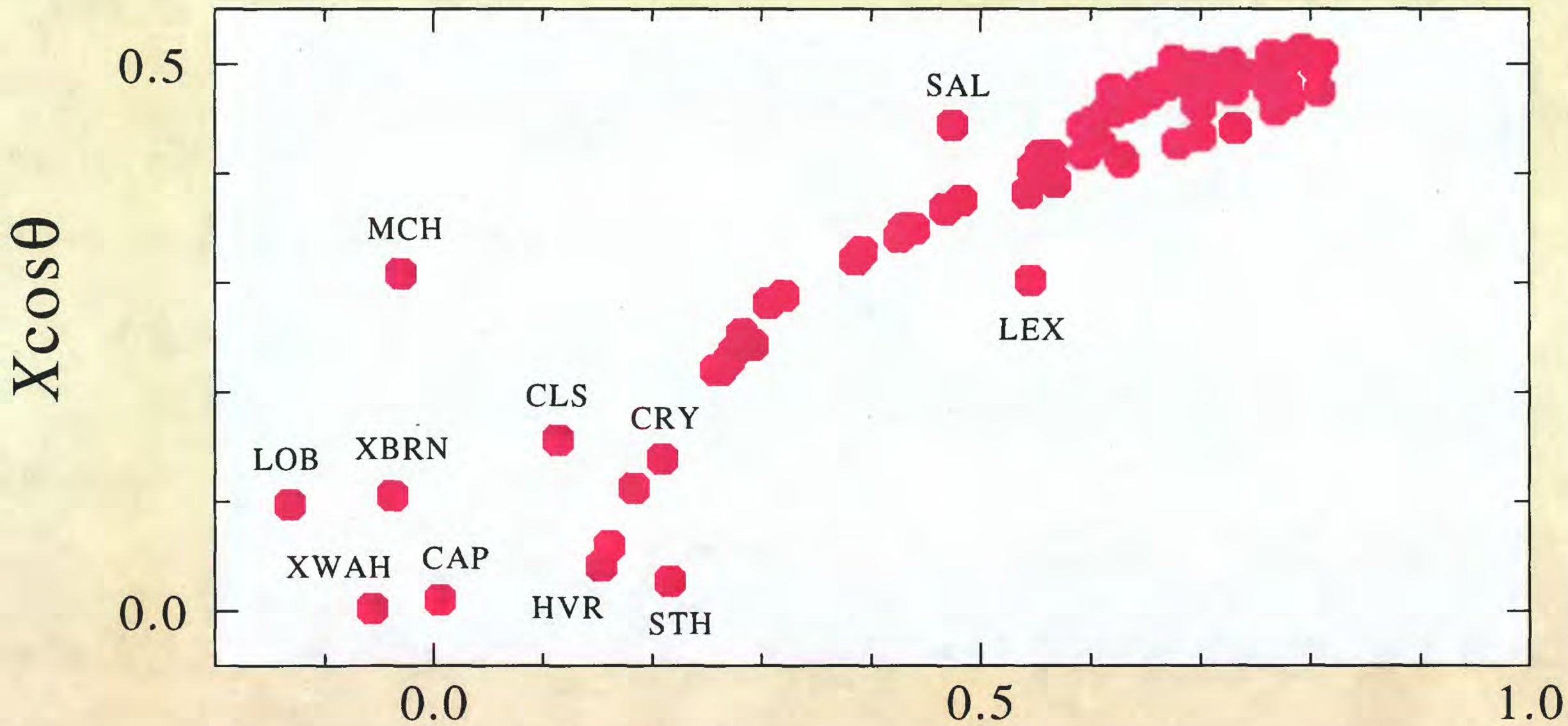

$X\cos\theta$

$\langle\cos\theta\rangle$ for $\nu = 0.8\beta$

Figure 3

Response Spectral Amplification and Attenuation at 3.0 s

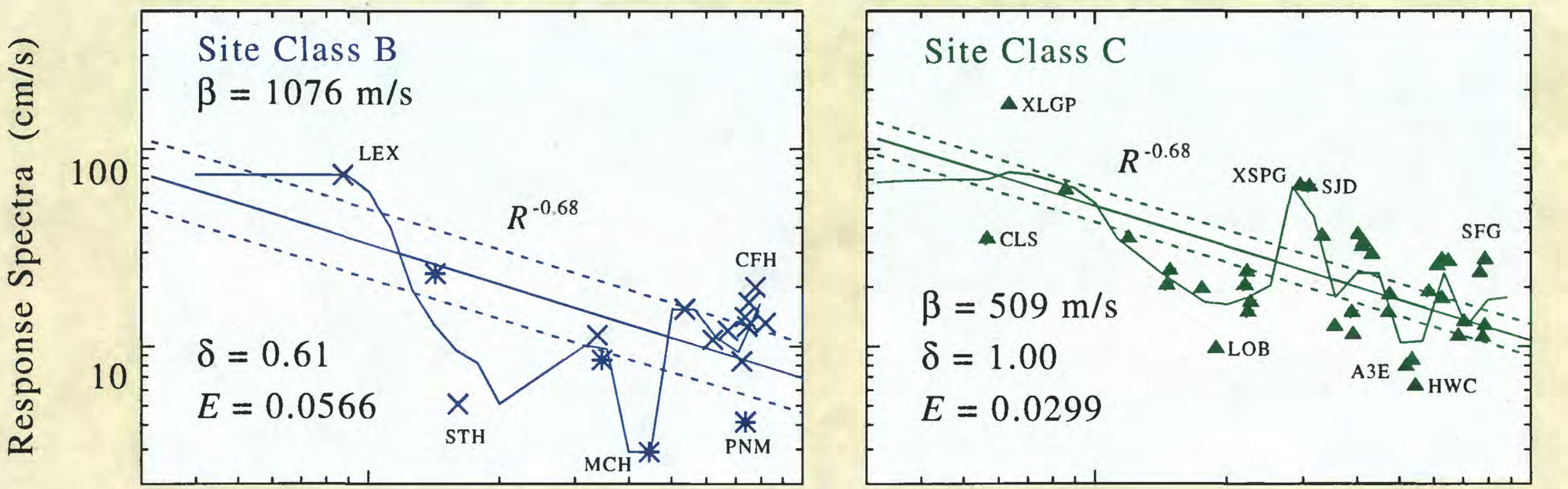

Figure 4a

Ground Motion Attenuation at 3 seconds

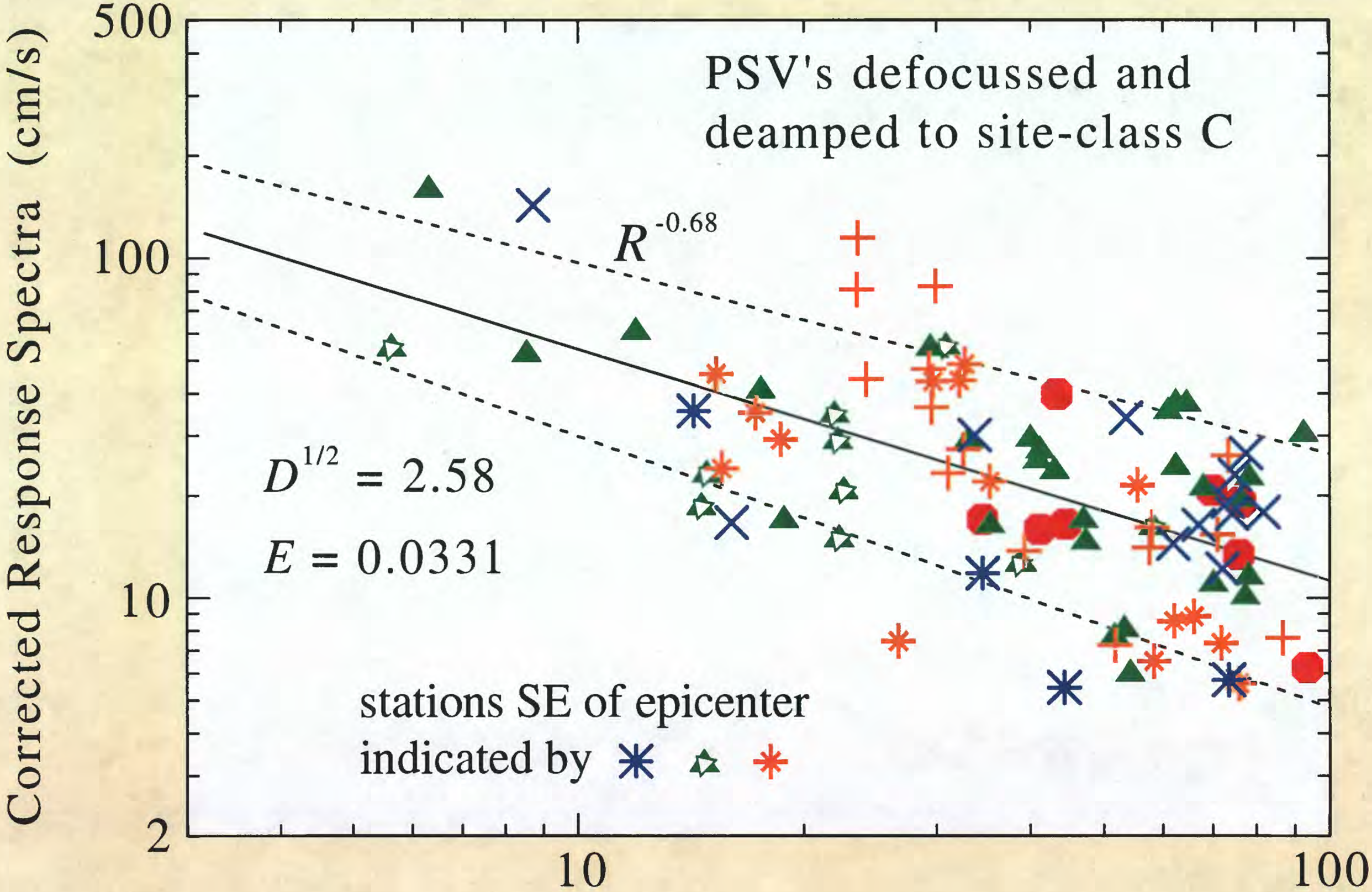

Figure 4b

Response Spectra at 30 km and 3 seconds

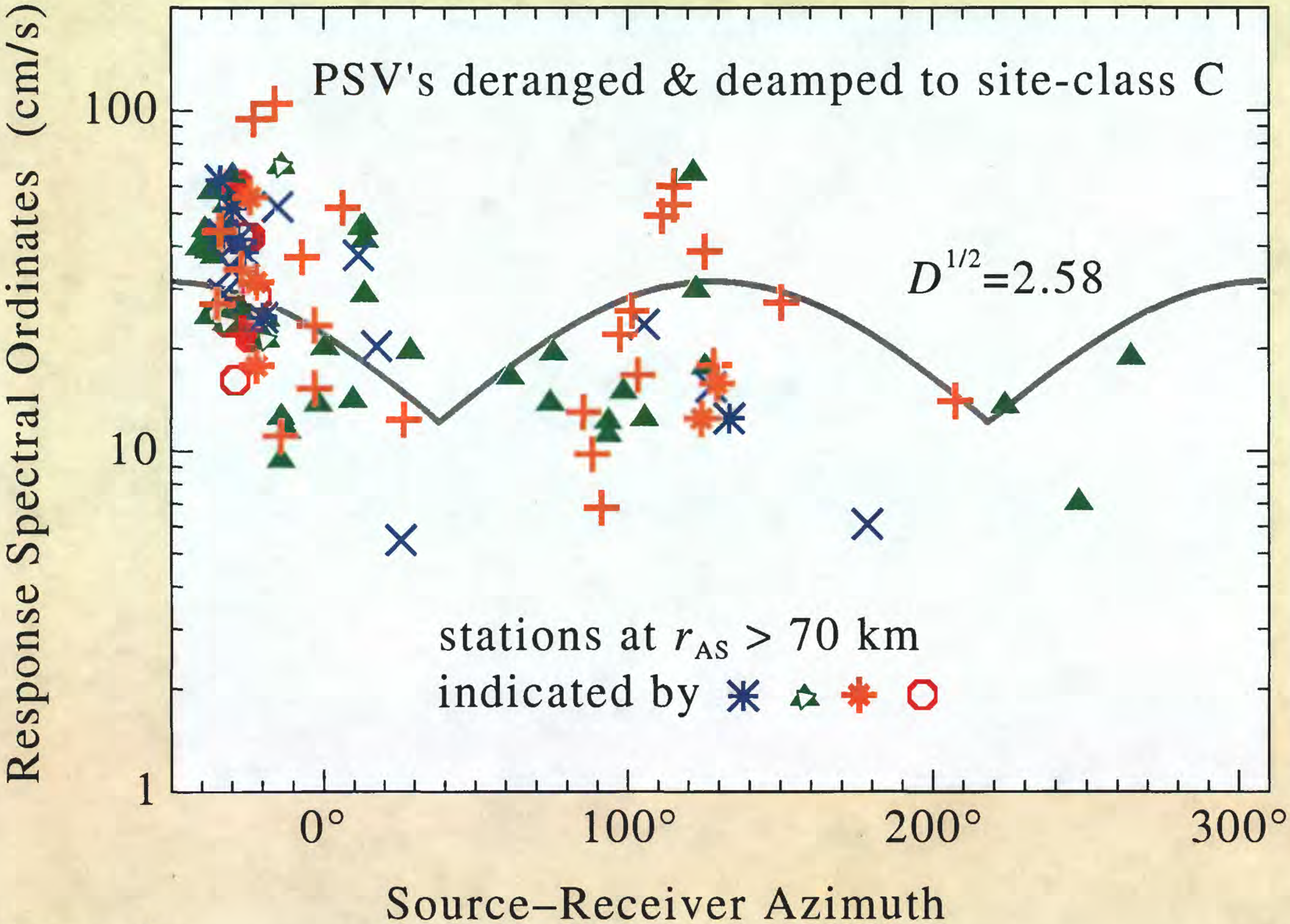

Figure 4c

Loma Prieta - Attenuation Exponent $(R^{-\gamma})$

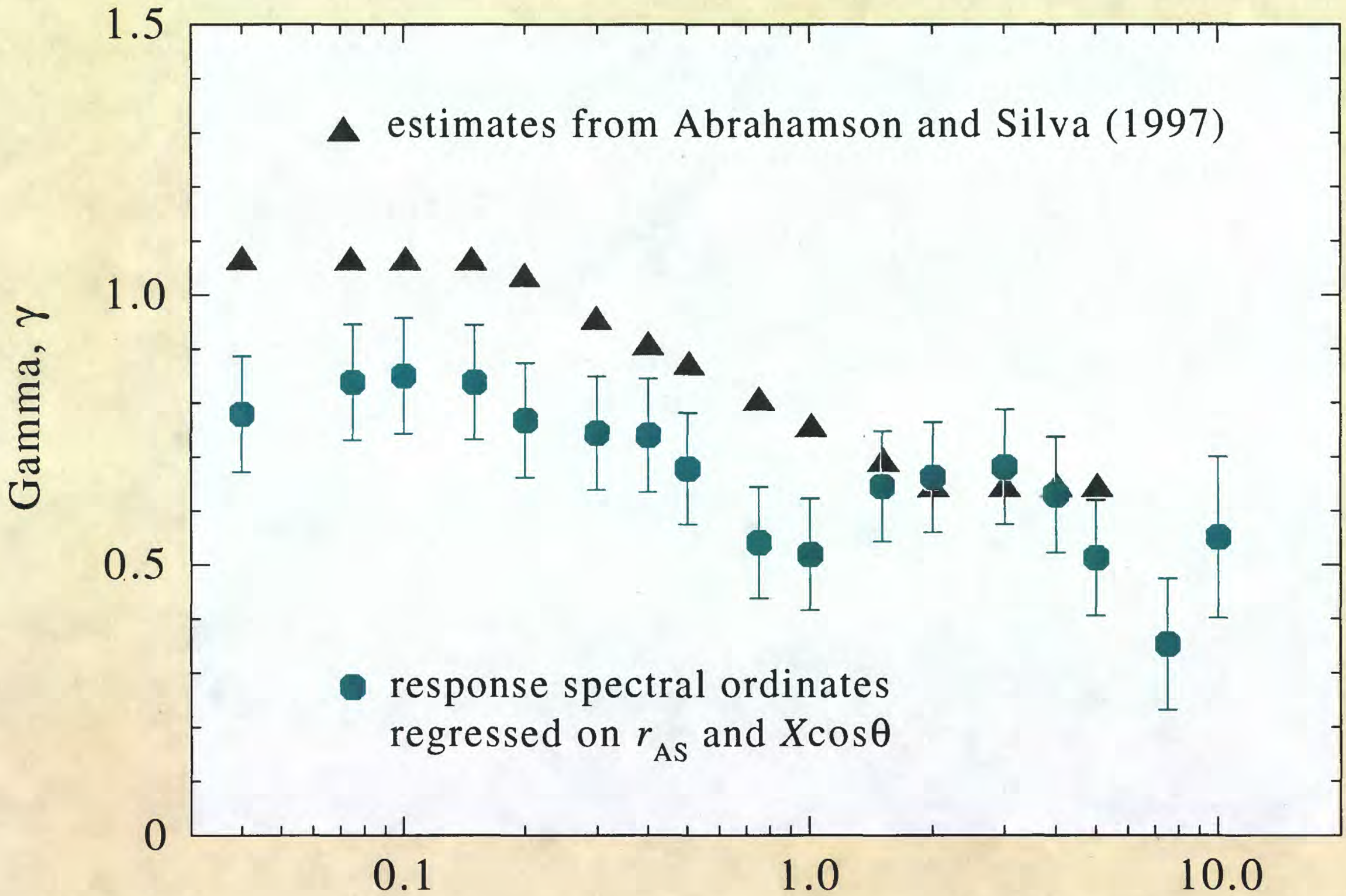

Figure 5

Loma Prieta - Directivity

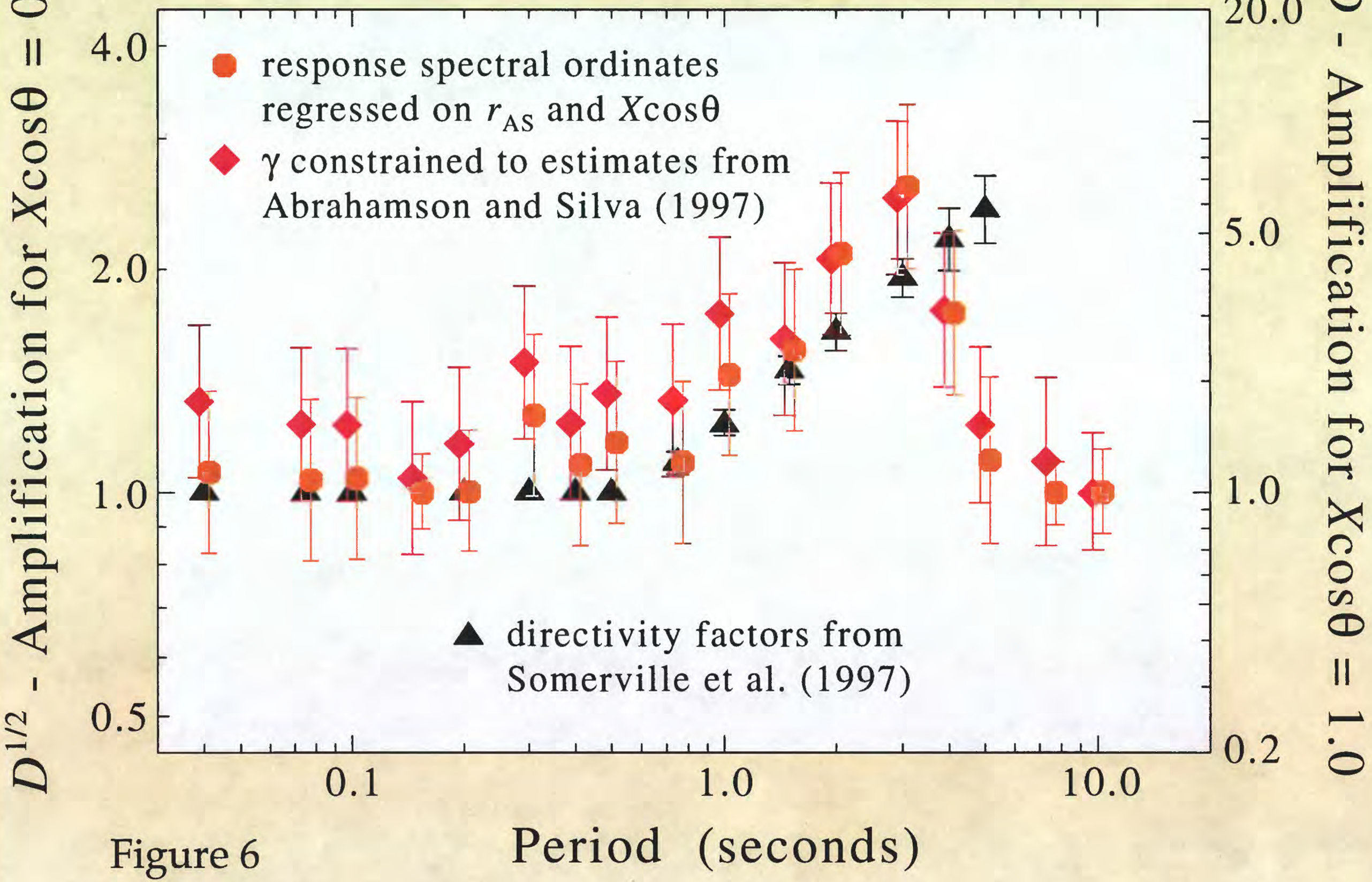

Figure 6

Amplification Regressed by Site Class

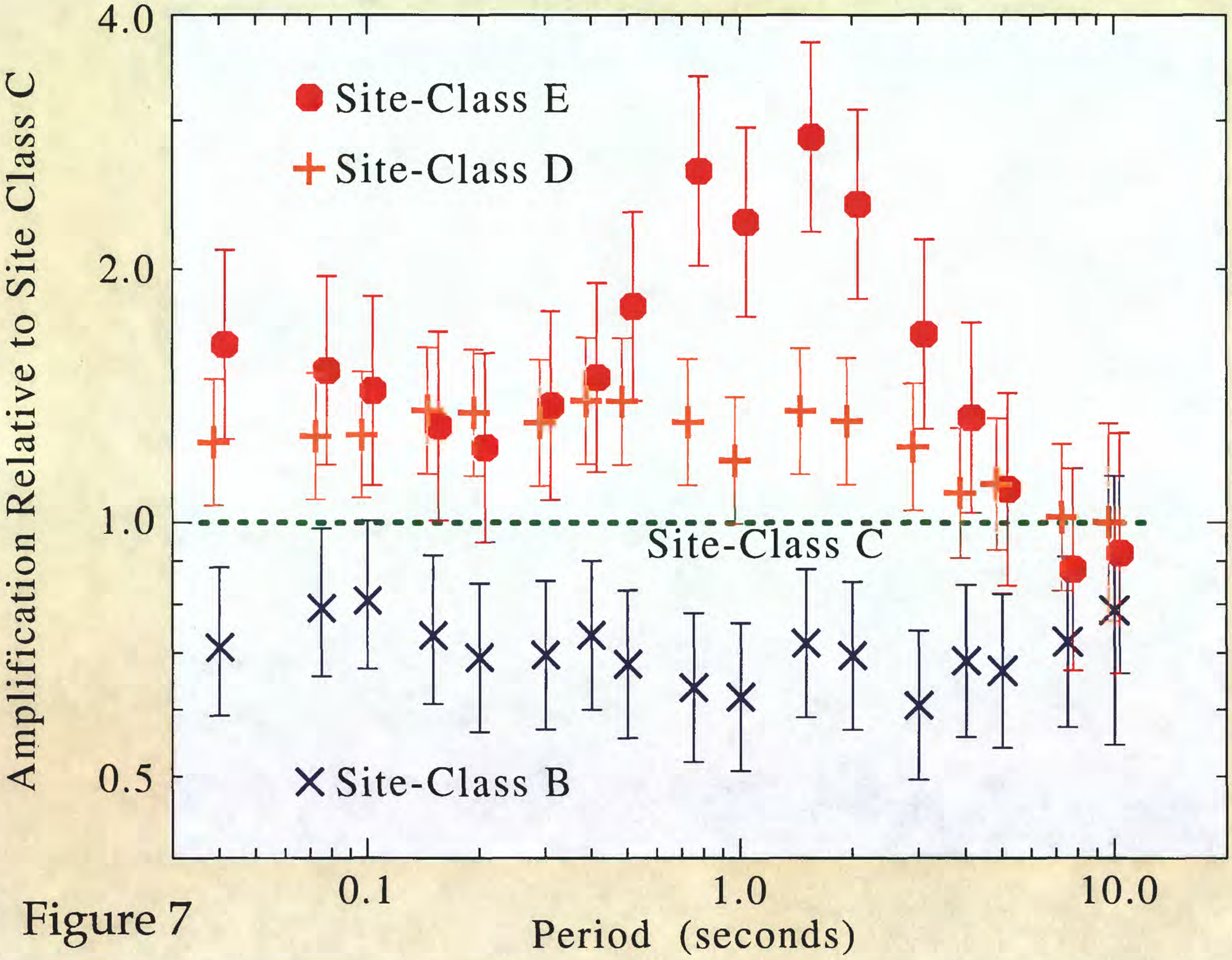

Figure 7

Loma Prieta - Attenuation Exponent $(R^{-\gamma})$

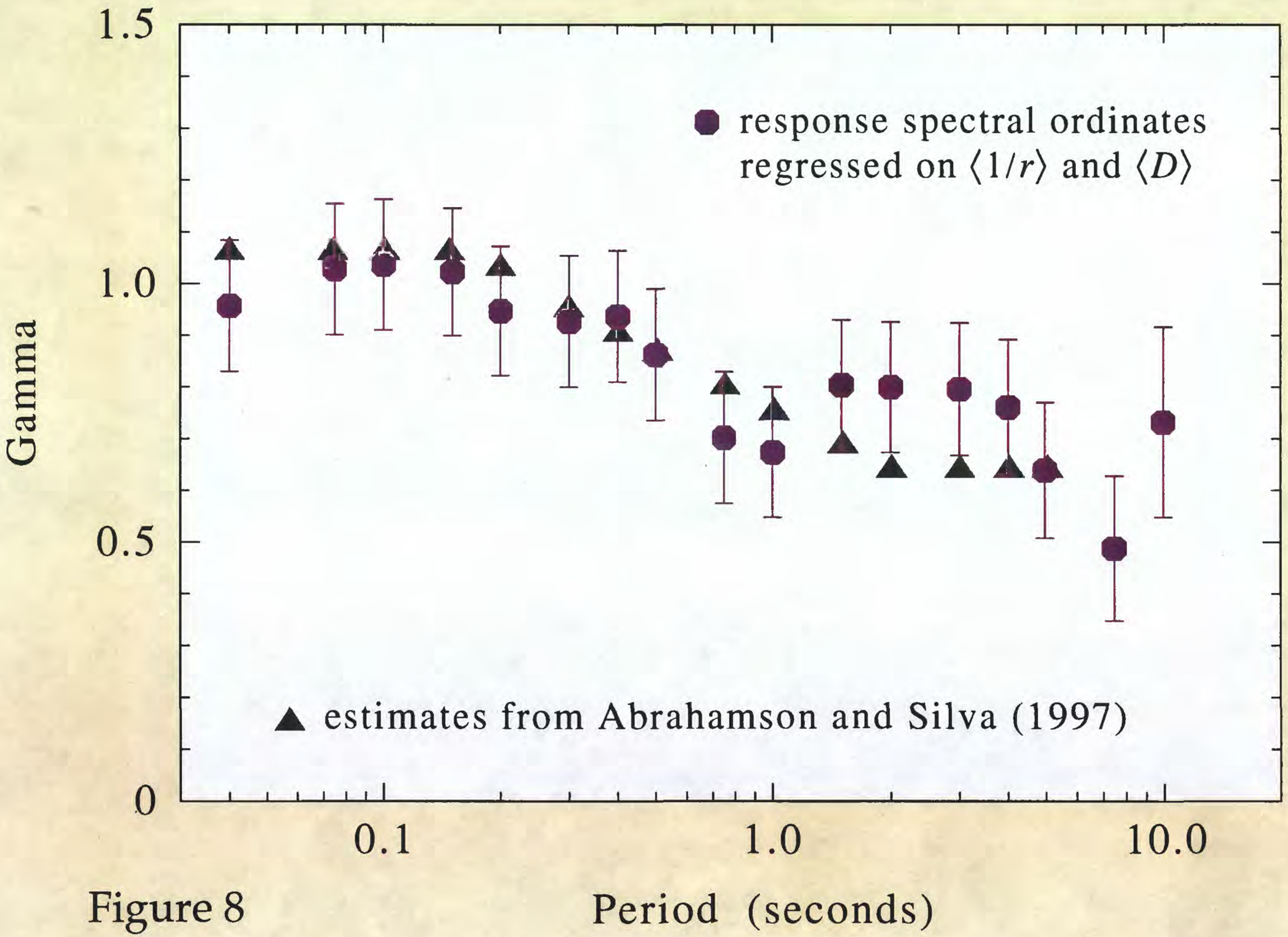

Figure 8

Loma Prieta - Response Spectra at $\langle 1/r \rangle^{-1}$ = 10 km

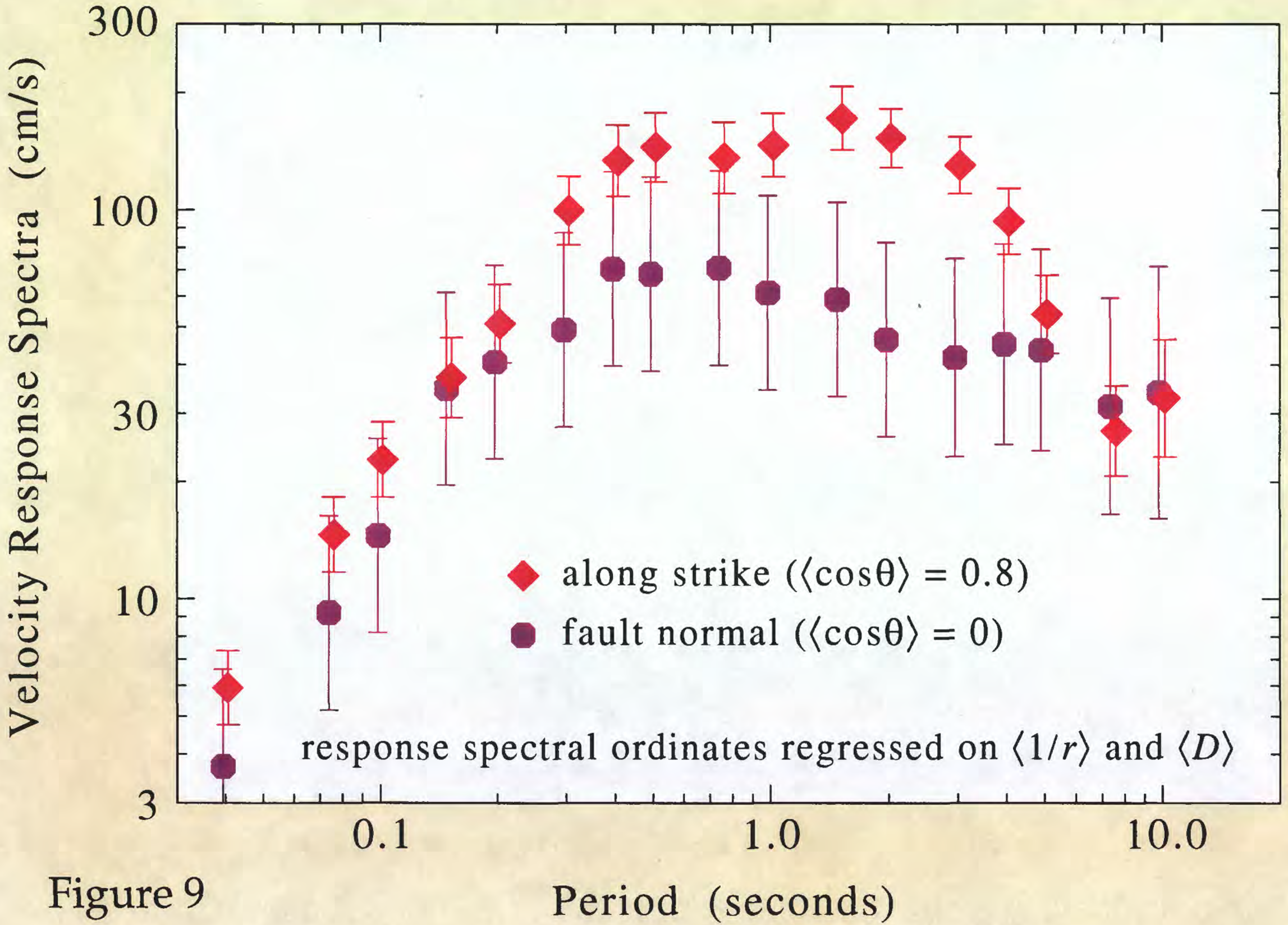

Figure 9

Loma Prieta - Directivity

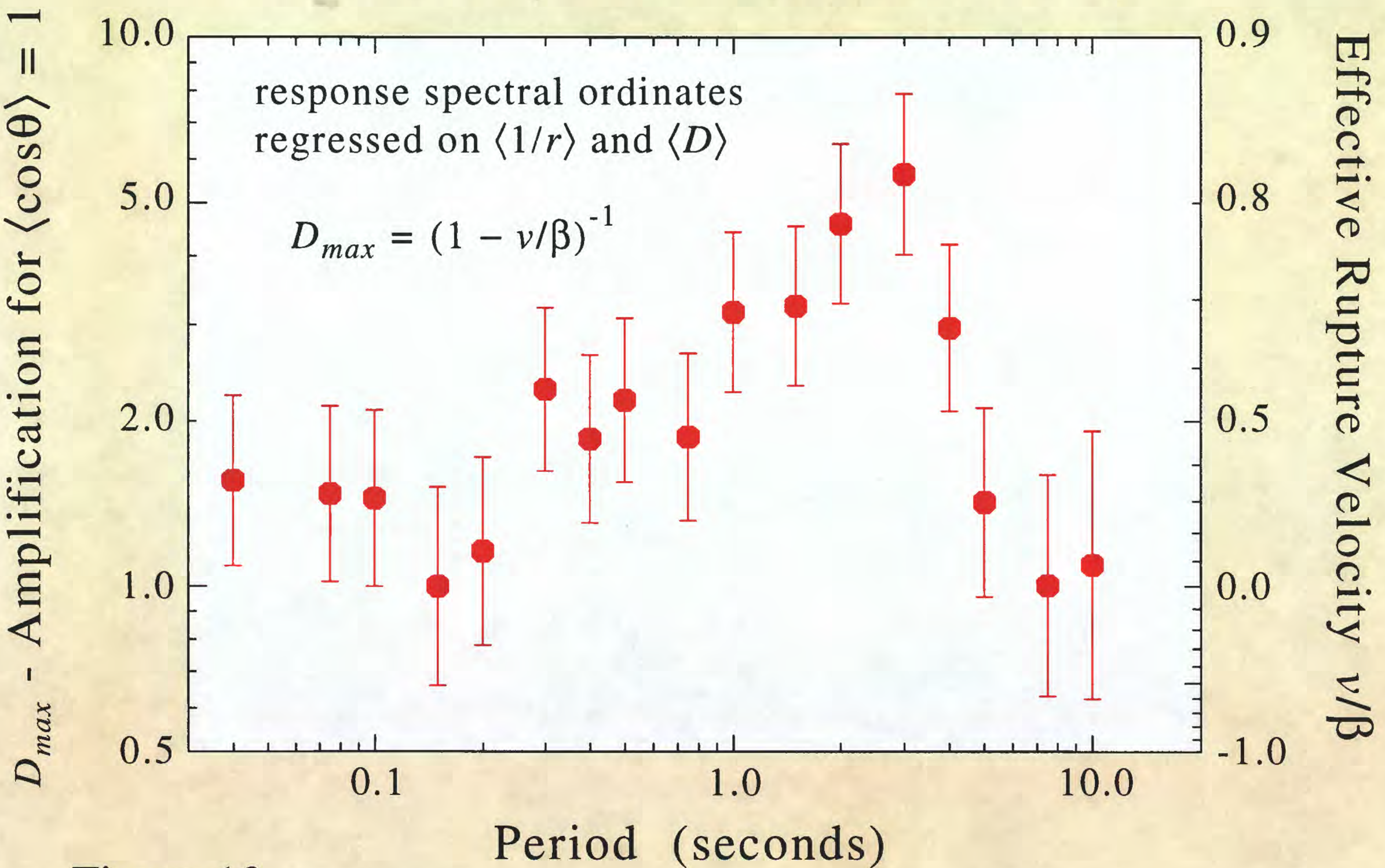

Figure 10